西安交通大學
XI'AN JIAOTONG UNIVERSITY

World Scientific
www.worldscientific.com

Microstructure regulation and failure mechanism study of BaTiO₃-based dielectrics for MLCC application

Yan Gu, Faqiang Zhang[*,‡], Wanghua Wu and Zhifu Liu[†,‡]

CAS Key Lab of Inorganic Functional Materials and Devices, Shanghai Institute of Ceramics
Chinese Academy of Sciences, Shanghai 200050, P. R. China

*zhangfq@mail.sic.ac.cn, †liuzf@mail.sic.ac.cn

Most widely used dielectrics for MLCC are based on BaTiO₃ composition which inevitably shows performance degradation during the application due to the migration of oxygen vacancies ($V_O^{\cdot\cdot}$). Here, the BaTiO₃, (Ba$_{0.97}$Ca$_{0.03}$)TiO₃, Ba(Ti$_{0.98}$Mg$_{0.02}$)O₃, (Ba$_{0.97}$Ca$_{0.03}$)(Ti$_{0.98}$Mg$_{0.02}$)O₃, (Ba$_{0.96}$Ca$_{0.03}$Dy$_{0.01}$)(Ti$_{0.98}$Mg$_{0.02}$)O₃ ceramics (denoted as BT, BCT, BTM, BCTM and BCDTM, respectively) were prepared by a solid-state reaction method. The core-shell structured grains (~200 nm) featured with 10–20 nm wide shell were observed and contributed to the relatively flat dielectric constant-temperature spectra of BTM, BCTM and BCDTM ceramics. The TSDC study found that the single/mix doping of Ca²⁺, especially the Mg²⁺, Mg²⁺/Ca²⁺ and Mg²⁺/Ca²⁺/Dy³⁺ could limit the emergence of $V_O^{\cdot\cdot}$ during the sintering and suppress its long-range migration under the electric-field. Because of this, the highly accelerated lifetimes of the ceramics were increased and the value of BCDTM is 377 times higher than that of BT ceramics. The *p-n* junction model was built to explain the correlation mechanism between the long-range migration of $V_O^{\cdot\cdot}$ and the significantly increased leakage current of BT-based dielectrics in the late stage of HALT.

Keywords: BaTiO₃-based dielectrics; failure mechanism; microstructure regulation; oxygen vacancies; leakage current.

1. Introduction

Multilayer ceramic capacitors (MLCCs) are widely used in modern electronics to realize the bypass, filtering, decoupling and energy storage functions.[1,2] The electric reliability of MLCCs is very important for the operation of the electron equipment. However, the performance degradation inevitably appeared during the application MLCCs.[3–5] So, to understand the mechanism and avoid or retard the degradation of MLCCs are the key topics for the product development of high-performance MLCCs.

Barium titanate BaTiO₃(BT)-based compounds, featured with high capacity, miniaturized size and low-cost advantages are currently the most applied dielectric material for MLCCs.[6–10] The performance degradation and failure behaviors of BT dielectrics significantly affect the electric reliability of MLCCs.[11] Numerous investigations suggested that it is oxygen vacancies migration from the anode to the cathode under the electric field that leads to the resistance degradation of BT-based dielectrics.[12–16] The field-induced migration of oxygen vacancies $V_O^{\cdot\cdot}$ usually can be detected by the thermally stimulated depolarization current (TSDC) test, which shows that the oxygen vacancies $V_O^{\cdot\cdot}$ can be activated at 100–200°C.[17] Experimentally, researchers found the migration of oxygen vacancies can be controlled in some ways. For example, the migration activation energy of the $V_O^{\cdot\cdot}$ was found to be closely

related to their existing forms (such as isolated defects, dipoles, or clusters)[7] and the crystal/grain orientation.[18] The Ba vacancies V_{Ba}'' induced by donor doping (such as Y³⁺, Dy³⁺, Ho³⁺, Er³⁺, La³⁺, etc.) were proven to trap the oxygen vacancies and hence increase the HALT lifetime.[19–21] Our study further showed that donor doping can also suppress the emergence of oxygen vacancies in the lattice.[22] Liu and co-workers studied the evolution of TSDC spectra during the highly accelerated lifetime test (HALT) and built the ionic demixing model to bridge the oxygen vacancies migration with resistance degradation.[23] They thought the oxygen vacancies (initially mobile or becoming free after dissociating from the defect dipoles) first move in the grain and accumulated at the grain boundaries. Then, once the oxygen vacancies start to migrate across grain boundaries and start to pile up near the cathode, a strong degradation of the insulation resistance occurs. The ionic demixing model successfully connects the resistance degradation evolution with the oxygen vacancies migration process. However, it is regrettable that the underlying physical mechanism of the formation of leakage current is still blurry.

In this study, we designed and prepared a series of typical BT-based dielectric ceramics by Ca/Mg/Dy doping to comparatively study the field-induced oxygen vacancy migration in different featured BT dielectrics. The TSDC, HALT and XPS were applied to analyze the degradation evolution

‡Corresponding authors.

characteristics. The physical model on the formation mechanism of leakage current and thermal breakdown was built.

2. Experimental

The $BaTiO_3$, $(Ba_{0.97}Ca_{0.03})TiO_3$, $Ba(Ti_{0.98}Mg_{0.02})O_3$, $(Ba_{0.97}Ca_{0.03})(Ti_{0.98}Mg_{0.02})O_3$, and $(Ba_{0.96}Ca_{0.03}Dy_{0.01})(Ti_{0.98}Mg_{0.02})O_3$ ceramics (respectively denoted as BT, BCT, BTM, BCTM and BCDTM, respectively) were prepared by a solid-state reaction method as described in our previous work.[24] The nanosized starting powders, $BaTiO_3$ (Sinocera, 99%, 200 nm), $CaCO_3$ (Sinocera, 99%, 500 nm), TiO_2 (Beijing Yili Fine Chemicals Co.,99%, 100 nm), Dy_2O_3 (Aladdin, 99.99%, 30–40 nm) and MgO (Aladdin, 99.9%, 20–30 nm), as the raw materials, were weighed according to the stoichiometric composition and wet ball-milled for 24 h in Nylon tanks with ethanol and zirconia balls. The dried slurries were pre-calcined at 1100°C for 2 h in an alumina crucible and then ball-milled for 6 h. After drying at 80°C, the calcined powers were pressed into disks with a diameter of 12 mm in diameter s at 50 MPa. Finally, these disks were debonded at 500°C for 2 h, and, then sintered at 1340–1390°C (BT) and 1380–1420°C (BCT, BTM, BCTM, BCTDM) for 4 h in air with furnace cooling. The samples sintered at 1360°C (BT) and 1400°C (BCT, BTM, BCTM, BCTDM) were found to have the maximum density (See Fig. S1) and hence were ground down to 0.5 mm in thickness for the following studying. The silver paste was printed on both sides of the samples and then fired at 600°C for 30 min to serve as electrodes.

The X-ray diffraction (XRD, Rigaku D/MAX 2550 V, Japan) was used to determine the phase structure of the samples. Raman spectra were measured at the wavenumber range of 100–1000 cm⁻¹ by a DXR Raman Microscope

(Thermo Scientific). The microstructure of sintered samples was observed using a scanning electron microscope (SEM, Hitachi S-4800). The core-shell structure of the grains was characterized by a field-emission transmission electron microscopy (FE-TEM, JEOL-2100-F) and the electron energy loss spectrometer (EELS) was performed as well. The dielectric properties were measured by using a Turnkey Concept 40 dielectric and impedance spectrometer (Novocontrol Technologies) at a temperature of −55–150°C. The impedance spectra were measured by a WayneKerr WK6500B impedance spectrometer over the range of frequencies from 20 Hz to 10 MHz at 300°C. The evaluation of each R (resistance) and C (capacitance) component value for a properly assumed equivalent RC circuit was determined by Zview software. Leakage current also was monitored at 150°C by applying a DC field of 1200 V mm⁻¹ for the HALT (Agilent 34970A, Agilent Technologies Inc., USA). TSDC measurement was performed by an electrometer/high resistance meter (KEITHLEY 6517B, Keithley Instruments, Inc., Cleveland, USA). X-ray photoemission spectroscopy (XPS) was measured by using a Physical Electronics PHI 5300 spectrometer with a nonmonochromatic Mg-Kα radiation (250 W, 14 kV) as the excitation source.

3. Results and Discussion

Figure 1(a) shows the X-ray diffraction patterns of the BT, BCT, BTM, BCTM and BCDTM ceramics at room temperature. The pure perovskite-structured phase was obtained in all samples. The doping effects on the lattice structure are revealed by the splitting state of (200) peak around $2\theta = 44°–46°$. As shown in the magnified spectra of Fig. 1(a), the obvious splitting of (200)/(002) peaks of BCT suggests the tetragonal structure of BCT like BT ceramic at room
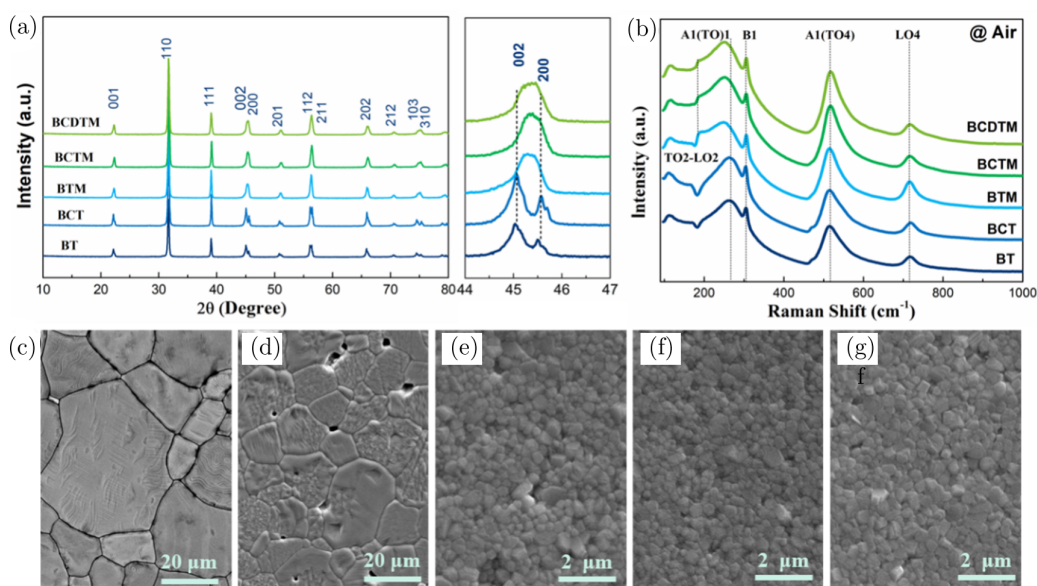

Fig. 1. (a) XRD spectra, (b) Raman spectra and (c)–(g) SEM images of the as-prepared $BaTiO_3$-based ceramics.

temperature. Differently, a single but un-sharp (200) peak was observed when the MgO was added. This feature indicates that the BTM, BCTM and BCDTM ceramics have a trend to form cubic structure, agreeing with the phenomenon that Mg^{2+} ions(0.72 Å) dope into Ti^{4+} sites (0.61 Å) as acceptors.[25] But it should note that the cubic structure is statistical and the un-sharp (200) peak demonstrates the poor lattice-ordering degree of BTM, BCTM and BCDTM ceramics. The Raman spectra of the as-prepared ceramics are given in Fig. 1(b). Four absorption bands around 270, 307, 519 and 718 cm^{-1} were observed, corresponding to the $A_1(TO_2)$, $B1+E(2LO+3TO)$, $A_1(3TO)+E(4TO)$ and $A_1(3LO)+E(4LO)$ modes of $BaTiO_3$, respectively.[26] Significant change can also be observed when MgO was added. The 270 cm^{-1} peaks become wider and move to lower wavenumber regions for BTM, BCTM and BCDTM ceramics, confirming the substitution of Mg^{2+} ions for Ti^{4+} ions to lead to the lattice distortion. Meanwhile, the emergence of the 195 cm^{-1} peaks after Mg-doping also proves that some Mg^{2+} ions enter into A sites. Hence, it can be speculated that the Mg^{2+} ion is an A/B sites codoped element in our case. The effect of doping on sintering and microtopography is shown in Figs. 1(c)–1(g). All the samples show a dense sintering state. Grains with 10–20 μm size were observed in BCT, slightly smaller than that of BT (15–30 μm) ceramic. Remarkably, when Mg^{2+} ions

were added, nanosized grains (~200 nm) were obtained for BTM, BCTM and BCDTM. This is because the Mg^{2+} ions can play the blocker role for grain growth in the sintering process of BT-based ceramics.[25]

To clear the sudden change of the sample containing Mg^{2+} on the XRD and Raman spectra, the grains of BCTM and BCDTM were characterized by TEM. As shown in Figs. 2(a) and 2(b), all of the grains in BCTM and BCDTM manifest the core–shell structure feature and the width of the shell layer is about 10–20 nm. The EELS line-scanning results (Fig. 2(c)) of the grain marked in Fig. 2(b) reveal that the doping elements are mainly concentrated in the shell layers and the doping content in the cores is almost zero, thus the un-sharp (200) diffraction peak of BTM, BCTM and BCDTM can be understood. It can be speculated that the core–shell grain structure should be the main difference between the BTM/BCTM/BCDTM ceramics and BT/BCT ceramics (Fig. 2(d)). Such a remarkable change on grain structure must be further reflected in the dielectric properties of the samples. Indeed, as shown in Fig. 2(e), relatively flat dielectric constant-temperature spectra can be observed for BTM, BCTM and BCDTM while typical spectra with obvious phase transition peaks were detected for BT and BCT ceramics. For BTM, BCTM and BCDTM ceramics, two blurry Curie phase transition peaks corresponding to the core and shell layers, respectively,
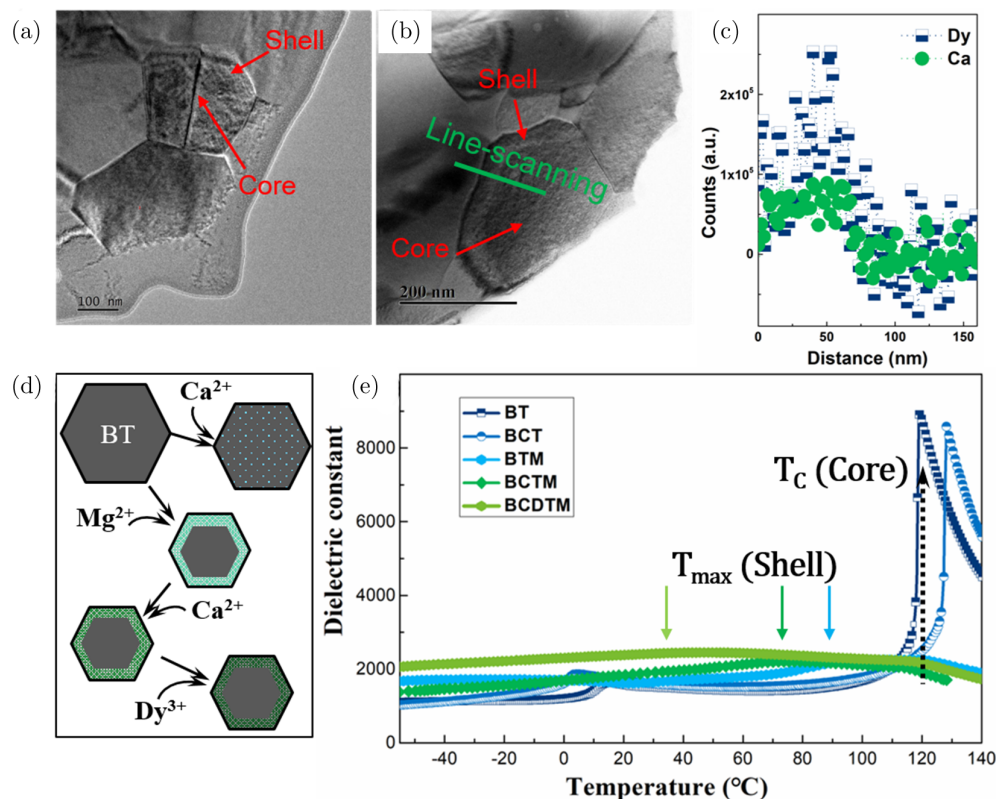

Fig. 2. (a) and (b) TEM image of BCTM and BCTDM ceramic. (c) EELS line-scanning results of Dy and Ca elements cross the grain boundary of BCDTM ceramic. (d) Diagram of the grain-structure evolution process with doping elements. (e) Temperature dependence of dielectric constant.
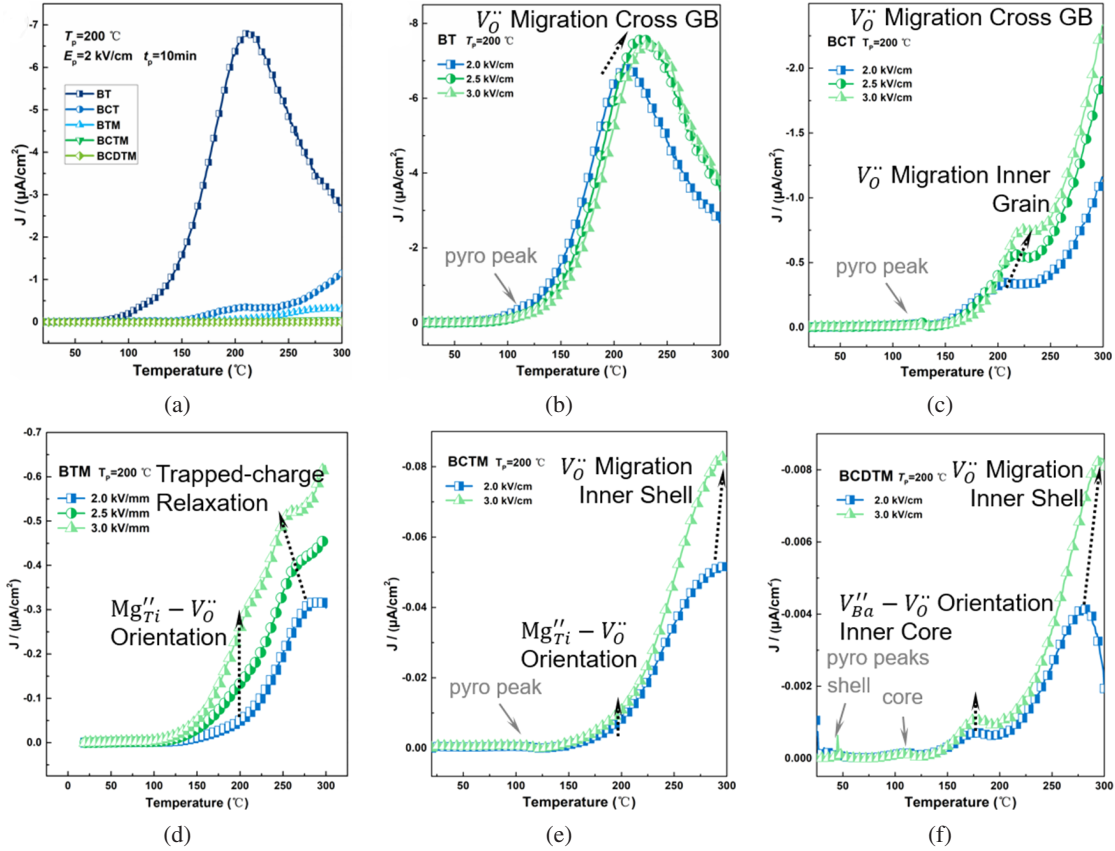
Fig. 3. (a) TSDC spectra of as-prepared samples under polarization at $T_p = 200°C$ and $E_p = 2.0$ kV/mm. (b)–(f) TSDC spectra of BT, BCT, BTM, BCTM and BCDTM ceramics under polarization at $E_p = 2.0$–3.0 kV/mm.

can be distinguished. The peak positions of these three samples at high temperatures are consistent with each other and almost overlap with the Curie phase transition peak of BT, suggesting the Curie phase transition of cores. Due to the doping effect of Ca/Mg/Dy, the Curie phase transition temperatures of the shells were reduced to different degrees for BTM, BCTM and BCDTM ceramics, thus the floating Curie phase transition peaks (T_{max}) were observed. The composite effect of core and shell creates the relatively flat dielectric constant-temperature spectra of BTM, BCTM and BCDTM. This is exactly why commercial BT-based dielectric materials and MLCC can be used in a wide temperature range. Here, the typical and changed features of BT, BCT, BTM, BCTM and BCDTM ceramics on multi-scale microstructure and dielectric properties give us good materials to comparatively study the electric reliability and failure mechanism of BT-based dielectric ceramics.

Figure 3(a) gives the TSDC spectra of the as-prepared samples with different depolarization current peaks. Generally, the depolarization current peaks in BT-based dielectrics are mainly related to the multiform polarization behaviors of oxygen vacancies ($V_O^{\cdot\cdot}$), thus the current density could reflect the $V_O^{\cdot\cdot}$ content in the ceramics. It can be seen that the current peak value of pure BT ceramic reaches -7 μA/cm^2, which is unexpectedly higher than that of the H$_2$/Ar-annealed BT single

crystal (about -1.5 μA/cm^2) in our previous work, suggesting the number of $V_O^{\cdot\cdot}$ that emerges during the sintering process is enormous.[18] But, as shown in Fig. 3(a), it is fortunate that the doping effect of Ca/Mg/Dy could significantly suppress the emergence of $V_O^{\cdot\cdot}$. To respectively understand the action rule of Ca/Mg/Dy, the existing states of $V_O^{\cdot\cdot}$ in the samples were analyzed by testing the TSDC spectra after polarizing under different electric-field (E_P) at 200°C. As shown in Fig. 3(b), the main TSDC peak of BT ceramic is at 200–250°C and increases with the rise of E_P. This phenomenon agrees well with the long-range migration feature of $V_O^{\cdot\cdot}$, revealing the very weak bound state of $V_O^{\cdot\cdot}$ and the low grain-boundary (GB) barrier of pure BT ceramics. When CaO was added, the main long-range migration peak moved to a higher temperature (out of the test range of the device) and a sub-long-range migration emerges (Fig. 3(c)). The main peak corresponds to the migration across the GB while the sub-peak represents the migration inside the grains. This result indicates that the CaO doping could increase the GB-barrier of BT ceramic but the majority of $V_O^{\cdot\cdot}$ are still relatively free in the sample. In contrast, as shown in Fig. 3(d), the main current peak of BTM ceramics almost moves to disappear and change to two sub-current peaks. The peak near 200°C shows an independent feature with E_P and can be speculated to correspond to the orientation-depolarizing of defect dipoles $Mg_{Ti}'' - V_O^{\cdot\cdot}$.[23]

$$O_O \rightleftharpoons \tfrac{1}{2}O_2 + V_O^{\cdot\cdot} + 2e' \ (1) \qquad Ba_{Ba} + O_O \rightleftharpoons V_{Ba}'' + V_O^{\cdot\cdot} + \text{``}BaO\text{''} \ (2)$$

Oxygen Vacancy Arising in Grain-growth Process

$\odot V_O^{\cdot\cdot}$ $\bullet V_{Ba}''$

Local Lattice Adjusting
$$Ba_{Ba} + CaO \rightleftharpoons Ca_{Ba} + \text{``}BaO\text{''} \ (3)$$

MgCa

Raw Defect

Mg

Raw Defect

MgCaDy

$\bullet Mg_{Ti}''$
$\bullet\!-\!\odot$ Defect Dipole

$Dy_{Ba}^{\cdot}$
$\odot\!-\!\bullet\!-\!\odot$ Defect Network

Depolarization Direction   **Oxygen Vacancy Creating**   **Oxygen Vacancy Suppressing**

$\nearrow$

$$MgO + Ti_{Ti} + O_O \rightleftharpoons (Mg_{Ti}'' + V_O^{\cdot\cdot}) + O_2 \ (4) \qquad MgO + Dy_2O_3 + Ti_{Ti} + Ba_{Ba} \rightleftharpoons (Mg_{Ti}'' + 2Dy_{Ba}^{\cdot}) + 2O_2 \ (5)$$
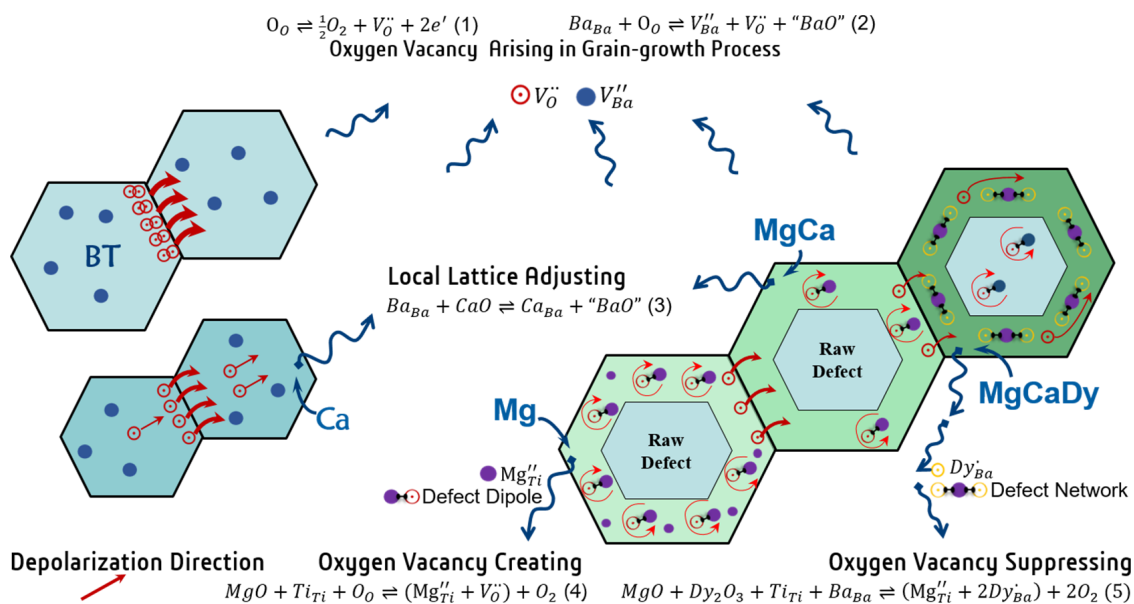
Fig. 4. The schematic diagram of the defects forming and oxygen vacancies migration behavior in the depolarization process of TSDC test.

The position of the peak near 260°C decreases with the rise of E_P, a typical feature of trapped-charge depolarization,[23] hence is considered to be induced by Mg_{Ti}''. The emergence of these two peaks suggests that Mg_{Ti}'' could well constrain the $V_O^{\cdot\cdot}$ by forming defect dipoles and there is certain excess for Mg_{Ti}''. As shown in Fig. 3(e), the doping state of Mg^{2+} seem to be changed when the Ca^{2+} ions were added to BMT. The depolarization peaks of defect dipoles $Mg_{Ti}''/V_O^{\cdot\cdot}$ and trapped-charge near Mg_{Ti}'' were suppressed, while the long-range migration peak emerges again. Considering the migration across GB was moved to a much higher temperature for BCT and BMT ceramic, we speculated that this peak may correspond to the long-range migration of $V_O^{\cdot\cdot}$ inside the shell layers. Furtherly, as shown in Fig. 3(f), while the Dy^{3+} ions were added, the depolarization current of the long-range migration of $V_O^{\cdot\cdot}$ inside the shell layers were suppressed to about one-tenth of BCTM ceramics, indicating the reducing content of $V_O^{\cdot\cdot}$ in shell layers. In such a situation, the very weak orientation-depolarizing current peak of raw defect dipoles show $V_{Ba}'' - V_O^{\cdot\cdot}$ emergencies.

Here, the results of TSDC analysis were further integrated. As shown in Fig. 4, the $V_O^{\cdot\cdot}$-related defect reactions of Eqs. (1) and (2) are activated during the grain-growth process in the sintering, hence the undoped "grow regions" are the weaknesses that significantly affect the reliability of BT-based dielectrics (Fig. 3(a)).[18] For pure BT ceramic, the reactions accumulate to a very high magnitude in the grain and due to the GB-barrier being almost negligible, the depolarization current peaks of $V_O^{\cdot\cdot}$ migration in the grain and cross the GB merge to form a wide TSDC peak. When small-sized Ca^{2+} ions were added, Eq. (3) will take place and adjust the local lattice. The shrinkage of local lattice would suppress Eqs. (1) and (2), hence reducing the concentration of $V_O^{\cdot\cdot}$. Additionally,

maybe due to the element segregation in GB, the GB-barriers are raised and the TSDC spectrum shows typical double peaks feature corresponding $V_O^{\cdot\cdot}$ long-range migration in the grain and cross the GB. Different from the equivalent element doping of Ca^{2+} at Ba^{2+} sites, Mg^{2+} ions occupying Ti^{4+} sites would create $V_O^{\cdot\cdot}$ to balance the local charge (Eq. (4)).[27] The oxygen vacancies ($V_O^{\cdot\cdot}$) here are significantly constrained by Mg^{2+} ions and can only jump between the adjacent O^{2-} sites near the Mg^{2+} ions due to the strong electrostatic force in defect dipole ($Mg_{Ti}'' - V_O^{\cdot\cdot}$).[23] For this reason, the orientation-depolarizing current peak of defect dipoles and the peak of trapped-charge in the defect dipoles are observed in Fig. 3(d). For BCTM ceramics, due to the adjusting role of Ca^{2+} on the local lattice, the doping sites of Mg_{Ti}'' may be partially modulated to Ba^{2+} site[24] and the orientation-polarizing behavior is also suppressed due to the shrinking local lattice. Thus, as shown in Fig. 3(e), the orientation-depolarizing current peak fades away and leaves the weak long-range migration current peak of isolated oxygen vacancies ($V_O^{\cdot\cdot}$). Furthermore, Dy^{3+} doping would suppress the emergence of the balance-oxygen vacancies ($V_O^{\cdot\cdot}$) and form a defect network ($Dy_{Ba}^{\cdot} - Mg_{Ti}'' - Dy_{Ba}^{\cdot}$), which could strongly constrain the migration of $V_O^{\cdot\cdot}$ and thus significantly reduce the TSDC current.[22] As a complementary evidence for above speculation, Fig. 2(s) gives the complex impedance spectra (measured at 300°C) of BCT, BTM, BCTM and BCDTM ceramics. Two distinct impedance circles could be observed for BCT ceramic while the complex circles were detected for BTM, BCTM and BCDTM ceramics. The R-CPE circuits were used to fit the spectra and the resistance components are shown in Table 1. Due to the existence of the shell layer, an extra circle could be fitted. The shell resistance values (0.2–2.55 MΩ) are much higher than that of the core resistance (0.01–0.02 MΩ) and increase by

Table 1. The flitting resistance values of each electric part of BCT, BTM, BCTM and BCDTM ceramics at 300°C.

Samples	Rg(MΩ)		
	Rgc(MΩ)	Rgs(MΩ)	Rgb(MΩ)
BCT	0.21		0.97
BTM	0.01	0.20	2.18
BCTM	0.02	1.17	7.27
BCDTM	0.02	2.55	14.40

Ca and Dy doping. Meanwhile, the improved grain boundary resistances could be fitted, suggesting the important role of grain boundary except the grain shell.

As shown in Fig. 5(a), the HALT was used to investigate the reliability of the as-prepared samples. The time-dependent leakage currents were detected and HALT conditions of temperature and electric-field are 150°C and 1200 V/mm, respectively. It can be seen that the critical phenomenon was observed in all samples and the rapid increase of leakage current suggests the failure of the samples (Fig. 5(b)). In addition, the Ca/Mg/Dy doping significantly increases the HALT life of BT ceramics. For BCDTM, the life is even up to 723 min and is 377 times higher than that of the un-doped BT ceramics. The change rules of HALT lifetimes of BT/BCT/BTM/BCTM/BCDTM are in keeping with the trends of TSDC peaks shown in Fig. 3(a), confirming the dependence of performance degradation on oxygen vacancies migration. The results of the XPS spectrum near the cathode of BCDTM ceramic that aged for 0 h, 26 h and 51 h give the macro accumulative effect of oxygen vacancies migration. According to the valence bond model,[28] the valence state of Ti element is the sum of the bond valence of Ti–O bonds and it is usually +4. Due to the missing oxygen ion in $V_O^{\cdot\cdot}$, the adjacent Ti ion would be in the under-valence state inevitably and Ti^{3+} ions could be detected. As shown in Figs. 5(c) and 5(d), with the increase of aging time, the ratio of $S(Ti^4)/S(Ti^3)$ decreased gradually from 2.38 to 0.66, revealing the macro migration of $V_O^{\cdot\cdot}$ under electric field. Hence, it can be speculated that the failure of the samples must have close relations with the macroaccumulative effect of oxygen vacancies migration.

Why the macroaccumulative effect of oxygen vacancies migration would lead to a significant increase in leakage current? To clarify this question, the ionic and electronic states of the aged sample were further discussed. As shown in Fig. 6(a), under the electric field, defect dipoles are destroyed and separated relatively due to the long-range migration of $V_O^{\cdot\cdot}$. In the late stage of aging, the sample could be divided into two different areas from the cathode to the anode.[23,29] The $V_O^{\cdot\cdot}$ defects dominate the dielectric layers near the cathode, while the V_{Ba}''/Mg_{Ti}'' defects control the rest of the dielectric area. It is noted that the $V_O^{\cdot\cdot}$ is *n*-type defect while V_{Ba}''/Mg_{Ti}'' is the *p*-type defect for BT ceramic hence, as shown in Fig. 6(b), the two areas can also be described as donor-region and acceptor-region. The macrostructure of the aged-BT is such that its ceramic is exactly like the *p-n* junction in semiconductors. This gave us a question: Is it possible that the aged-BT ceramic is a *p-n* junction? To verify this hypothesis, we measured the *I-V* curve of the aged-BCTM ceramic. As shown in Fig. 6(c), the *I-V* curve similar to that of a *p-n* junction was detected. When the forward electric field was applied, a large current was tested and increased with the rise of the electric
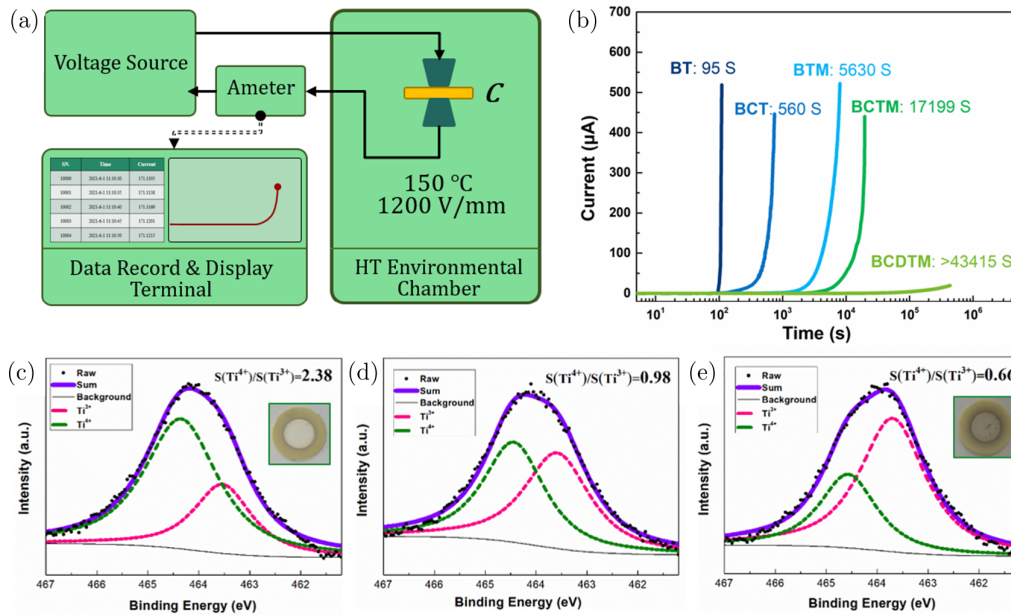

Fig. 5. (a) Schematic diagram of the HALT device configuration. (b) HALT curves of the as-prepared ceramics. (c)–(e) Raw and fitted Ti 2p$^{1/2}$ XPS spectra of the BCDTM ceramics that were aged for 0 h, 26 h and 51 h under HALT conditions.
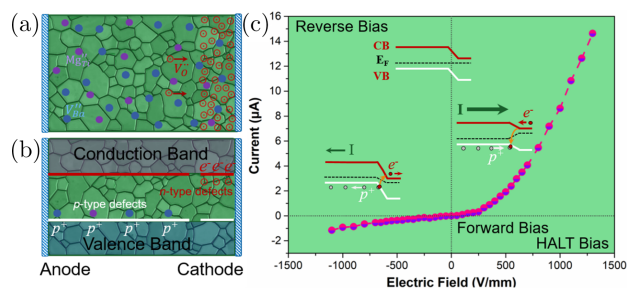
Fig. 6. (a) Diagram of Defects distribution and $V_O^{\cdot\cdot}$ accumulation state in BT-based dielectrics after thorough aging treatment. (b) The corresponding energy-band diagram. (c) *I-V* curve of BCTM ceramics after aging under 1200 V/mm, 150°C and 18 h. The energy-band diagrams at different biases are also given.

field. In contrast, when the reverse bias was applied, the current become very weak. This feature confirms the formation of *p-n* junction during the HALT of BT-based dielectrics. Meanwhile, it is noted that the HALT electric field is exactly along the forward bias of the *p-n* junction, hence the leakage current could flow through the *p-n* junction freely and even lead to breakdown when an over-large electric field was applied. So, a *p-n* model was put forward to explain the aging and failure of BT-based MLCC dielectrics. In the model, the aging process of BT-based dielectric under an electric-field comes with the destruction of the defect dipoles and the long-range migration of $V_O^{\cdot\cdot}$, which leads to the formation of the macro *p-n* junction. Due to the net donor and acceptor defect doping, the conductivities of *p-* and *n-* regions increase and, driven by the HALT electric field, the large leakage current forms and flows through the junction freely. Ultimately, a stable leakage current (low HALT electric field condition test) or electro-thermal breakdown (high HALT electric field condition test) would be observed. Both the stable leakage current and breakdown in the late stage of HALT had also been reported by former researchers,[29,30] confirming the reasonability of the *p-n* junction model.

4. Conclusion

In summary, the BaTiO$_3$, (Ba$_{0.97}$Ca$_{0.03}$)TiO$_3$, Ba(Ti$_{0.98}$Mg$_{0.02}$)O$_3$, (Ba$_{0.97}$Ca$_{0.03}$)(Ti$_{0.98}$Mg$_{0.02}$)O, (Ba$_{0.96}$Ca$_{0.03}$Dy$_{0.01}$)(Ti$_{0.98}$Mg$_{0.02}$)O$_3$ ceramics (denoted as BT, BCT, BTM, BCTM and BCDTM, respectively) were prepared by a solid-state reaction method to comparatively study the field-induced oxygen vacancy migration in BT-based dielectrics with different microstructures. The BTM, BCTM and BCDTM ceramics were found to have the core–shell structured nanograins and the doping elements mainly distributed in the shell layers. The TSDC tests showed that the doping of Ca^{2+}, especially the Mg^{2+}, Mg^{2+}/Ca^{2+} and Mg^{2+}/Ca^{2+}/Dy^{3+} could limit the emergence of $V_O^{\cdot\cdot}$ and suppress its long-range migration under the electric-field. The lifetime of BCDTM ceramics under the HALT condition reaches 723 min and is

377 times higher than that of the BT ceramics. A *p-n* junction model was put forward based on the macrodistributions of donor and acceptor defects in the aged samples. The long-range migration of oxygen vacancies would lead to the separating of donor and acceptor defects and forming the *p-n* junction. The forward HALT electric field in the *p-n* junction further leads to the large leakage current or performance failure of the dielectrics.

Supplemental Materials

The Supplemental Materials are available at: https://www.worldscientific.com/doi/suppl/S2010135X23500029.

References

[1] G. F. Yao, X. H. Wang, T. Y. Sun and L. G. Li, Effects of CaZrO$_3$ on X8R nonreducible BaTiO$_3$-based dielectric ceramics, *J. Am. Ceram. Soc.* **94**, 3856 (2011).

[2] L. X. Lin, J. Y. Yu, Y. R. Liu, N. Zhang and J. X. Chen, Synthesis and characterization of high performance CaZrO$_3$-doped X8R BaTiO$_3$-based dielectric ceramics, *Ceram. Int.* **41**, 8696 (2015).

[3] Y. A. Genenko, J. Glaum, M. J. Hoffmann and K. Albe, Mechanisms of aging and fatigue in ferroelectrics, *Mater. Sci. Eng. B* **192**, 52 (2015).

[4] D. Z. Xue, J. H. Gao, L. X. Zhang, H. X. Bao, W. F. Liu, C. Zhou and X. B. Ren, Aging effect in paraelectric state of ferroelectrics: Implication for a microscopic explanation of ferroelectric deaging, *Appl. Phys. Lett.* **94**, 082902 (2009).

[5] Y. Y. Zhao, J. P. Wang, L. X. Zhang, C. C. Wang and S. J. Liu, Aging rate of cerium doped Ba(Ti$_{0.99}$Mn$_{0.01}$)O$_3$, *Ceram. Int.* **43**, S70 (2017).

[6] C. S. Chen, C. C. Chou and I. N. Lin, Microstructures of X7R type base-metal-electroded BaTiO$_3$ capacitor materials prepared by duplex-structured process, *J. Eur. Ceram. Soc.* **25**, 2743 (2005).

[7] H. L. Gong, X. H. Wang, S. P. Zhang, Z. B. Tian and L. G. Li, Electrical and reliability characteristics of Mn-doped nano BaTiO$_3$-based ceramics for ultrathin multilayer ceramic capacitor application, *J. Appl. Phys.* **112**, 114119 (2012).

[8] D. Wang, Z. Fan, G. Rao, G. Wang, Y. Liu, C. Yuan, T. Ma, D. Li, X. Tan, Z. Lu, A. Feteira, S. Liu, C. Zhou and S. Zhang, Ultrahigh piezoelectricity in lead-free piezoceramics by synergistic design, *Nano Energy* **76**, 104944 (2020).

[9] H. Yang, Z. Lu, L. Li, W. Bao, H. Ji, J. Li, A. Feteira, F. Xu, Y. Zhang, H. Sun, Z. Huang, W. Lou, K. Song, S. Sun, G. Wang, D. Wang and I. M. Reaney, Novel BaTiO$_3$-based, Ag/Pd-compatible lead-free relaxors with superior energy storage performance. *ACS Appl. Mater. Interf.* **12**, 43942 (2020).

[10] R. Muhammad, A. Ali, J. Camargo, M. Castro, W. Lei, K. Song and D. Wang, Enhanced thermal stability in dielectric properties of NaNbO$_3$–modified BaTiO$_3$–BiMg$_{1/2}$Ti$_{1/2}$O$_3$ ceramics for X9R-MLCC applications. *Crystals* **12**, 141 (2022).

[11] H. Natsui, T. Shibahara, Y. Yonezawa and O. Kido, Effect of vanadium addition on reliability and microstructure of BaTiO$_3$-based

multilayer ceramic capacitors, *Jpn. J. Appl. Phys.* **51**, 09LC09 (2012).

[12]L. X. Zhang and X. B. Ren, Aging behavior in single-domain Mn-doped BaTiO$_3$ crystals: Implication for a unified microscopic explanation of ferroelectric aging, *Phys. Rev. B* **73**, 094121 (2006).

[13]Q. C. Zhao, H. L. Gong, X. H. Wang and L. T. Li, Investigation of improved reliability in BaTiO$_3$-based ceramics via two-step sintering by impedance spectroscopy and schottky barrier model, *Phys. Status Solidi A* **215**, 1800168 (2018).

[14]H. W. Lee, M. S. H. Chu and H. Y. Lu, Phase mixture and reliability of BaTiO$_3$-based X7R multilayer ceramic capacitors: X-ray diffractometry and raman spectroscopy, *J. Am. Ceram. Soc.* **94**, 1556 (2011).

[15]H. L. Gong, X. H. Wang, Q. C. Zhao and L. G. Li, Effect of Mg on the dielectric and electrical properties of BaTiO$_3$-based ceramics, *J. Mater. Sci.* **50**, 6898 (2015).

[16]H. L. Gong, X. H. Wang, S. P. Zhang, X. Y. Yang and L. G. Li, Influence of sintering temperature on core-shell structure evolution and reliability in Dy modified BaTiO$_3$ dielectric ceramics, *Phys. Status Solidi A* **211**, 1213 (2014).

[17]S. H. Yoon, C. A. Randall and K. H. Hur, Correlation between resistance degradation and thermally stimulated depolarization current in acceptor (Mg)-doped BaTiO$_3$ submicrometer fine-grain ceramics, *J. Am. Ceram. Soc.* **93**, 1950 (2010).

[18]W. H. Wu, Z. F. Liu., Y. Gu, Z. X. Yue and Y. X. Li, Thermally stimulated depolarization current study on barium titanate single crystals, *AIP Adv.* **8**, 045005 (2018).

[19]T. Tateishi, S. Suzuki, K. Banno and A. Ando, Effect of La doping on the suppression of insulation resistance degradation in multilayer ceramic capacitors, *Jpn. J. Appl. Phys.* **58**, SLLC02 (2019).

[20]M. Nagayoshi, K. Matsubara and N. Fujikawa, Analyses of microstructure at degraded local area in Ni-multilayer ceramic capacitors under highly accelerated life test, *Jpn. J. Appl. Phys.* **59**, SPPC01 (2020).

[21]A. Kirianov, T. Hagiwara, H. Kishi and H. Ohsato, Effect of Ho/Mg ratio on formation of core-shell structure in BaTiO$_3$ and on dielectric properties of BaTiO$_3$ ceramics, *Jpn. J. Appl. Phys.* **41**, 6934 (2002).

[22]L. Chen, Q. Q. Fu, Z. J. Jiang, J. J. Xing, Y. Gu, F. Q. Zhang, Y. Jiang and H. Gu, Cathodoluminescence evaluation of the degradation of Mg, Ca and Dy Co-doped BaTiO$_3$ Ceramics, *J. Eur. Ceram. Soc.* **41**, 7654 (2021).

[23]W. Liu and C. A. Randall, Thermally stimulated relaxation in Fe-doped SrTiO$_3$ systems: II. Degradation of SrTiO$_3$ dielectrics, *J. Am. Ceram. Soc.* **91**, 3251 (2008).

[24]Z. C. Yang, Y. Gu, F. Q. Zhang, Z. F. Liu and Y. X. Li, Improved dielectric breakdown strength of Dy doped (Ba$_{0.97}$Ca$_{0.03}$)(Ti$_{0.98}$Mg$_{0.02}$)O$_3$ ceramics with nanosized grains, *Phys. Status Solidi (A)* **214**, 1700149 (2017).

[25]J. Jeong and Y. H. Han, Effects of MgO-doping on electrical properties and microstructure of BaTiO$_3$, *Jpn. J. Appl. Phys.* **43**, 5373 (2004).

[26]S. Wada, M. Yano, T. Suzuki and T. Noma, Crystal structure of barium titanate fine particles including Mg and analysis of their lattice vibration, *J. Mater. Sci.* **35**, 3889 (2000).

[27]Y. Umeda, K. Masuzawa, S. Ueda, S. Ootsuki, A. Kuwabara and H. Moriwake, Theoretical and experimental analysis for site preference of rare earth elements in BaTiO$_3$, *Ceram. Int.* **38**, S25 (2012).

[28]J. P. Naskar, S. Hati and D. Datta, New bond-valence sum model, *Acta Crystallograph. B. Struct. Sci.* **53**, 885 (1997).

[29]T. Baiatu, R. Waser and K. H. Hardtl, Dc electrical degradation of perovskite-type titanates: 3. A model of the mechanism, *J. Am. Ceram. Soc.* **73**, 1663 (1990).

[30]W. Liu, G. Y. Yang and C. A. Randall, Evidence for increased polaron conduction near the cathodic interface in the final stages of electrical degradation in SrTiO$_3$ crystals, *Jpn. J. Appl. Phys.* **48**, 051404 (2009).